

On the Vertical Structure of Mesoscale Eddies in the Kuroshio-Oyashio Extension

Hengkai Yao¹, Chao Ma¹, and Zhao Jing¹

¹Ocean University of China

July 31, 2023

Abstract

Vertical structure of mesoscale eddies is key to the eddy-induced heat/material transport that further affects the climate and marine ecosystem. This study explores the vertical structure of mesoscale eddies in the Kuroshio-Oyashio Extension region (KOE) and its underlying dynamics. By applying the hierarchical ascending classification to the observational and reanalysis datasets, we classify mesoscale eddies with three distinct kinds of vertical structures. Each kind of eddies exhibits clear spatial aggregation along a distinct zonal band. Eddies have core depths of 100-300 m in the northern part of the KOE and core depths of 300-500 m and 0-100 m in the southern. The eddy splitting or merging does not introduce new kind of eddy vertical structure but causes large intra-kind variability. The different kinds of eddy vertical structures can be partially accounted for by the inference from the baroclinic instabilities at the eddy generation sites.

Hosted file

969714_0_art_file_11227424_ry57nz.docx available at <https://authorea.com/users/644096/articles/657132-on-the-vertical-structure-of-mesoscale-eddies-in-the-kuroshio-oyashio-extension>

Hosted file

969714_0_supp_11227469_ryr7z0.docx available at <https://authorea.com/users/644096/articles/657132-on-the-vertical-structure-of-mesoscale-eddies-in-the-kuroshio-oyashio-extension>

1 **On the Vertical Structure of Mesoscale Eddies in the Kuroshio-Oyashio Extension**
2

3 **H. Yao¹, C. Ma¹, and Z. Jing^{1,2}**

4 ¹Physical Oceanography Laboratory, Ocean University of China, Qingdao, China.

5 ²Laoshan Laboratory, Qingdao, China.

6 Corresponding author: Chao Ma (machao@ouc.edu.cn)

7 **Key Points:**

- 8 • Three vertical structures of mesoscale eddies are classified in the Kuroshio-Oyashio
9 Extension region.
- 10 • Mesoscale eddy splitting or merging causes significant variation of vertical eddy
11 structures.
- 12 • Different vertical eddy structures can be partially accounted for by differences in baroclinic
13 instabilities.
14

15 **Abstract**

16 Vertical structure of mesoscale eddies is key to the eddy-induced heat/material transport that
17 further affects the climate and marine ecosystem. This study explores the vertical structure of
18 mesoscale eddies in the Kuroshio-Oyashio Extension region (KOE) and its underlying dynamics.
19 By applying the hierarchical ascending classification to the observational and reanalysis datasets,
20 we classify mesoscale eddies with three distinct kinds of vertical structures. Each kind of eddies
21 exhibits clear spatial aggregation along a distinct zonal band. Eddies have core depths of 100-300
22 m in the northern part of the KOE and core depths of 300-500 m and 0-100 m in the southern. The
23 eddy splitting or merging does not introduce new kind of eddy vertical structure but causes large
24 intra-kind variability. The different kinds of eddy vertical structures can be partially accounted for
25 by the inference from the baroclinic instabilities at the eddy generation sites.

26 **Plain Language Summary**

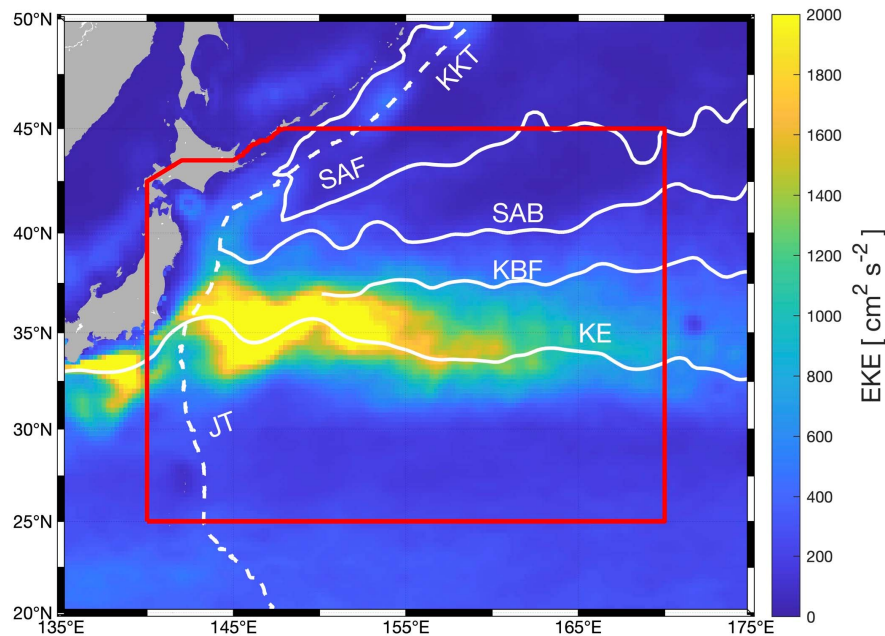
27 Mesoscale eddies are swirling motions with a radius ranging from several tens to a hundred of
28 kilometers. The mesoscale eddies can cause strong vertical displacement of isopycnals, yet the
29 vertical structure of such displacement has not been well understood. This study examines the
30 vertical structures of mesoscale eddies in the Kuroshio-Oyashio Extension region based on the
31 observational and reanalysis datasets. Mesoscale eddies with three distinct kinds of vertical
32 structures are identified.

33

34 **1 Introduction**

35 Mesoscale eddies are ubiquitous in the upper ocean. Although the surface signals of
36 mesoscale eddies have been well depicted based on satellite measurements, their vertical
37 structures are less understood yet play a critical role in the eddy-induced heat/material transport.
38 The latter has been shown to exert significant influences on the large-scale ocean thermal structure
39 (Yu et al., 2019), anthropogenic climate changes (Du et al., 2022), ocean's biogeochemical cycles
40 (McGillicuddy et al., 1998, 2007), dispersion of marine pollutants (Gilchrist et al., 2020) and
41 microplastics behavior (Cai et al., 2022).

42 The Kuroshio-Oyashio Extension (KOE) region, located near the western boundary of
43 North Pacific, consists of several prominent fronts including the subarctic front (SAF), the
44 subarctic boundary (SAB), the Kuroshio bifurcation front (KBF) and the Kuroshio extension (KE)
45 (Figure 1). The KOE region is characterized as a zone with elevated eddy kinetic energy (Qiu &
46 Chen, 2010; Figure 1) and also a hotspot for mid-latitude air-sea heat and carbon dioxide
47 exchanges (Fassbender et al., 2017; Jing et al., 2020). A knowledge of the vertical structure of
48 mesoscale eddies within the KOE region is thus essential for understanding the eddies' climate and
49 ecological impacts. By compositing all the mesoscale eddies around the KE front, Sun et al. (2017)
50 reported that the eddy core measured by density anomaly is on average located around 300-400 m.
51 In contrast, Dong et al. (2017) observed a deeper eddy core in the southern branch of the KE front
52 than the northern branch and attributed this vertical difference to the poleward shoaling of
53 thermocline. Ding and Jing (2020) analyzed the zonal variation of the eddy vertical structure,
54 identifying double-core eddies in the upper stream of the KE front.



55
 56 **Figure 1.** Climatological mean eddy kinetic energy (EKE; units: cm^2s^{-2}) from AVISO (Aviso Altimetry, 2022).
 57 Japan Trench (JT) and Kuril-Kamchatka Trench (KKT) are represented by the dashed white lines. The Subarctic
 58 Front (SAF), the subarctic boundary (SAB), the Kuroshio Bifurcation Front (KBF) and the Kuroshio Extension (KE)
 59 are represented by white thick lines and are recognized by AVISO mean dynamic topography (MDT) contour
 60 following Nakano et al., (2018). The red box is our research region.

61 Although these previous studies have advanced the understanding of eddy vertical
 62 structures in the KOE region, they suffer from several limitations. First, the previous studies dealt
 63 with the mean eddy vertical structure in some pre-defined subdomains of the KOE region. It
 64 remains elusive from such analysis how many there are distinct kinds of eddy vertical structures in
 65 the KOE region. Second, the previous studies analyzed the eddy vertical structure under a Eulerian
 66 framework and thus did not take into account the evolution of eddy vertical structure during the
 67 eddy life cycle. In particular, it is still unclear whether the eddy vertical structure would change
 68 significantly during the eddy splitting or merging process. Third, mesoscale eddies in the KOE
 69 region are generated primarily from the baroclinic instability especially for those large enough to
 70 be well identified from the satellite altimeters (Ji et al., 2018; Yang et al., 2018). A natural question
 71 is that to what extent the distinct eddy vertical structures in the KOE region can be accounted for
 72 by the baroclinic instability.

73 Recently, clustering techniques have been leveraged to analyze oceanic data (Sambe &
 74 Suga, 2022). Surface-intensified and subsurface-intensified eddies have been distinguished via the
 75 hierarchical ascending classification (HAC) for the four primary eastern boundary upwelling
 76 systems (Pegliasco et al., 2015). In contrast to traditional approaches that manually subdivide
 77 areas for analysis, the HAC is capable of offering an impartial classification of mesoscale eddies
 78 based on the mathematical similarity of their vertical structures.

79 In this study, we explore the vertical structure of mesoscale eddies in the KOE region under
 80 a Lagrangian framework, by applying the HAC to the observational and reanalysis datasets. The
 81 paper is organized as follows. Section 2 details the data and methods. The vertical structures of

82 mesoscale eddies as well as their changes during the eddy splitting or merging are documented in
83 Section 3. Section 4 discusses the role of baroclinic instability in shaping the eddy vertical
84 structure. The paper is ended with a summary of its major conclusions.

85 **2 Data and Methods**

86 2.1 Observational Data

87 Surface mesoscale eddies within the KOE region (135-175°E; 25-45°N) are detected and
88 tracked using daily maps of delayed-time multimission absolute dynamic topography (ADT) and
89 derived geostrophic velocity fields (UV) (Pujol, 2022). The data span a period of 22 years (from
90 January 2000 to December 2021) and have a spatial resolution of 1/4°. There are 3056 anticyclonic
91 eddies (AEs) and 3787 cyclonic eddies (CEs) detected and tracked in total via the TOEddies
92 algorithm (Laxenaire et al., 2019). Only mesoscale eddies possessing more than five Argo profile
93 within the maximum eddy velocity boundary during their lifespan are retained for further analysis.
94 After a quality control of the Argo data (see Supplementary Text S1), there are 6105 (3547) Argo
95 profiles in 394 AEs and 297 CEs used for analysis.

96 2.2 Reanalysis Data

97 Given the limitations in the spatio-temporal coverage of observational data, we have also
98 utilized the Four-Dimensional Variational Ocean Reanalysis for the Western North Pacific over 30
99 Years (FORA-WNP30) (Usui et al., 2017) to analyze the vertical structure of mesoscale eddies
100 and their underlying dynamics. The FORA-WNP30 offers a spatial resolution of 1/10° for the
101 majority of the research region, and 1/6° for the remainder. To align with the period during which
102 the assimilated altimeter-derived SSH was recorded, we only use model output from January 1993
103 to December 2014. From the FORA-WNP30 data, we detected and tracked 5100 AEs and 6371
104 CEs in total.

105 2.3 The Ocean Eddy Detection and Tracking Algorithms (TOEddies)

106 The TOEddies algorithm (Laxenaire et al., 2018, 2019), developed from the widely used
107 geometric algorithm (Chaigneau et al., 2008, 2009; Pegliasco et al., 2015), is used to detect and
108 track mesoscale eddies. The TOEddies algorithm does not only provide information on eddy
109 dynamical characteristics such as radius and velocity but also constructs a sophisticated eddy
110 network. This network connects eddy trajectories associated with merging with other eddies or
111 splitting into multiple eddies, enabling the tracking the origin of individual eddies.

112 Once an eddy is detected, eddy anomalies are calculated by subtracting a local
113 climatological mean profile. For the observational data, local climatological mean profiles of
114 potential temperature θ , salinity S and potential density σ are derived from the World Ocean
115 Atlas 2018 (WOA18) 1/4° objectively analyzed monthly climatology following Laxenaire et al.
116 (2020). These fields are linearly interpolated to match the position and day of the year of each
117 Argo float. For the reanalysis data, eddy anomalies are calculated by subtracting a large-scale
118 background field. The large-scale background of some variable, including θ , S , σ and horizontal
119 velocity (u, v) is first computed as its climatological mean seasonal cycle over a 22-year period.
120 Then this climatological mean seasonal cycle is further smoothed horizontally using a 41×41

121 grid boxcar filter and temporally using a 31-day running mean filter. The eddy kinetic energy
 122 (EKE) is computed as $EKE = (u'^2 + v'^2)/2$.

123 2.4 Cluster Analysis

124 To classify mesoscale eddies with different vertical structures, we implement the HAC
 125 technique following Pegliasco (2015) to eddies in the observational and reanalysis datasets. Due
 126 to the complexity of mesoscale eddies in the KOE region, the vertical profiles of $\theta'/S'/\sigma'$ at the
 127 centroids of the eddies and the average EKE profile along the SSH contour with the maximum
 128 eddy velocity are considered for a substantial classification.

129 All the vertical profiles are first linearly interpolated onto a 10-m regular grid from the
 130 surface to 1000 m, as the eddy signal below 1000 m in our research region is very weak. Then the
 131 vertical profiles of an eddy along its trajectory at different snapshots are averaged to form a single
 132 vertical profile. To remove potential obscure clusters classified by the HAC, following Laxenaire
 133 (2020) we discard weak eddies that have a maximum value of any vertical profile of $\theta'/S'/\sigma'$
 134 less than $0.1 \text{ } ^\circ\text{C}/\text{psu}/\text{kg m}^{-3}$. This criterion is applied to both the eddies in the observational and
 135 reanalysis data to keep consistency, yielding 394 (297) AEs (CEs) in the observational data and
 136 3130 (4001) AEs (CEs) in the reanalysis data. Note that the much smaller number of eddies in the
 137 observation is due to the sparsity of Argo profiles.

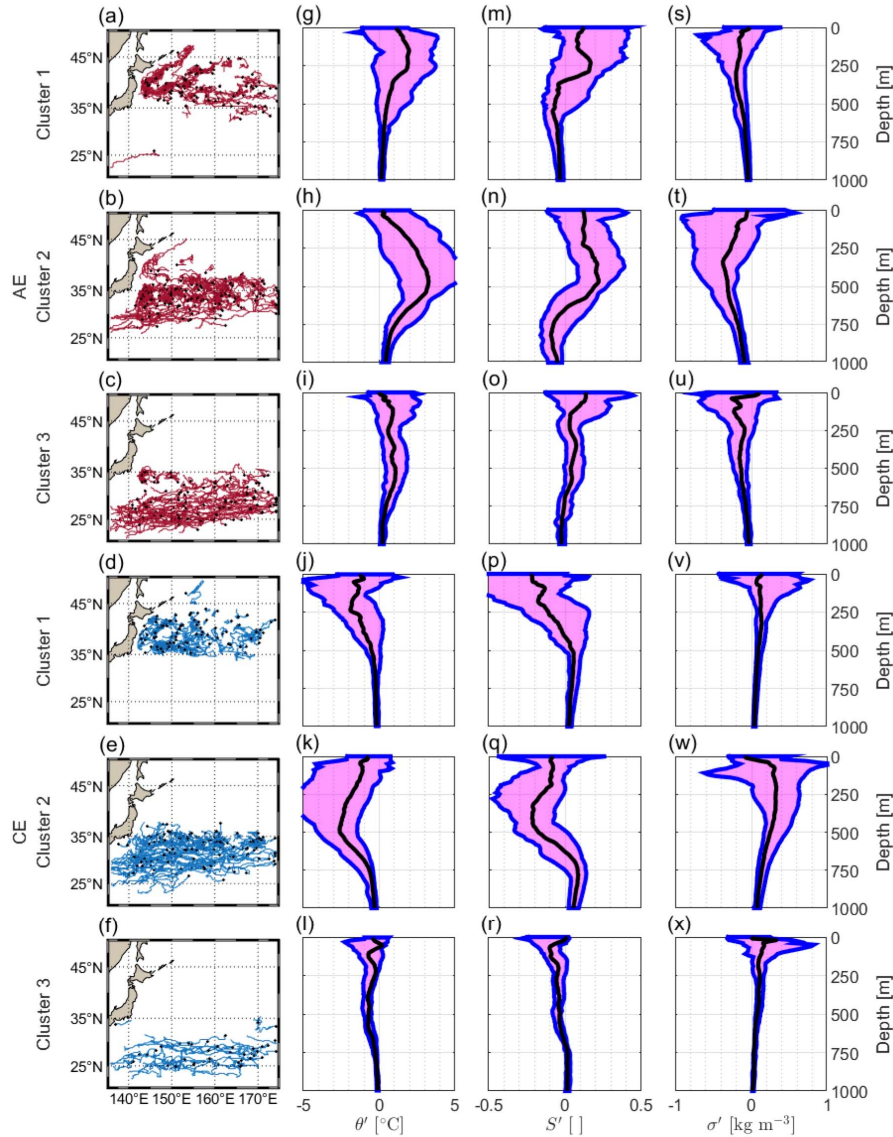
138 The HAC method first treats each eddy's vertical profiles of $\theta'/S'/\sigma'$ (and also EKE for
 139 the reanalysis data) as a unique cluster, subsequently merging similar clusters to form a unified
 140 cluster that encompasses all the eddies' vertical profiles. The merging process involves the three
 141 stages: calculating Euclidean distances of the normalized (dimensionless) vertical profiles
 142 between eddies; grouping closest eddies into a dendrogram using Ward's aggregation method
 143 (Ward, 1963); and finally selecting an optimal cut point in the cluster tree to best partition the
 144 eddies and retain significant clusters. Readers can refer to Pegliasso (2015) for more details of the
 145 HAC method.

146 3 Results

147 3.1 Vertical Structures of Mesoscale Eddies

148 Application of the HAC method to the observational data suggests that the vertical
 149 structures of AEs and CEs in the KOE region can be classified into three distinct clusters (Figure
 150 2). The first cluster, including 112 (28%) AEs and 117 (39%) CEs, is characterized by strong
 151 $\theta'/S'/\sigma'$ between 100 m and 300 m (Figure 2a, 2g, 2m, 2s, 2d, 2j, 2p and 2v). These eddies are
 152 predominantly located in the northern part (35°N - 45°N) of the KOE region. Tracking analysis
 153 reveals that many AEs and CEs in this cluster originate from the Subarctic Front (SAF), the
 154 Kuril-Kamchatka Trench (KKT) and downstream KE (Supplementary Figures S1 and S2). The
 155 AEs (CEs) included in this cluster tend to carry positive (negative) θ' and S' values with the
 156 former dominating σ' . The typical peaking values $\theta'/S'/\sigma'$ in the vertical are $1.97 \text{ } ^\circ\text{C}$, 0.17 psu ,
 157 and -0.20 kg m^{-3} for AEs and $-1.91 \text{ } ^\circ\text{C}$, -0.22 psu , and 0.15 kg m^{-3} for CEs, respectively. The
 158 water mass analysis implies that these eddies should carry Okhotsk Sea Mode Water (OSMW)
 159 (Yasuda, 1997; Gladyshev et al., 2003) and Transition Region Mode Water (TRMW) (Saito et al.,

160 2007), which is consistent with their origins derived from the tracking analysis (Supplementary
 161 Figure S3).



162 **Figure 2.** Spatial distributions and vertical structures ($\theta'/S'/\sigma'$) of eddies for each cluster in the observational data.
 163 (a-f) The trajectories of eddies (red/blue line indicate AEs/CEs, the black diamond markers show the birth location),
 164 vertical profiles of (g-l) potential temperature, (m-r) salinity and (s-x) potential density anomaly for each eddy
 165 clusters. The black curve in each functional boxplot (Genton & Sun, 2020; Sun & Genton, 2011) is the median
 166 profile and the magenta box is the 50% central region.
 167

168 The second cluster includes 164 (42%) AEs and 138 (46%) CEs, exhibiting strong
 169 $\theta'/S'/\sigma'$ between 300 m and 500 m (Figure 2b, 2h, 2n, 2t, 2e, 2k, 2q and 2w). This cluster is
 170 distributed around the center and to the south of the KE axis, located within the warm and salty
 171 region of the North Pacific Subtropical Mode Water (STMW) (Masuzawa, 1969) and Lighter
 172 Central Mode Water (L-CMW) (Oka et al., 2011) (Supplementary Figure S3). Some eddies in this
 173 cluster are shed off via the meandering of the KE (Ding & Jing, 2020), while others originate to the
 174 south of the KE axis or from the central North Pacific (Supplementary Figures S1 and S2). This

175 cluster displays typical peaking values of $\theta'/S'/\sigma'$ as 3.25 °C, 0.22 psu, and -0.38 kg m⁻³ for
 176 AEs and -2.62 °C, -0.22 psu, and 0.33 kg m⁻³ for CEs.

177 The third cluster comprises 118 (30%) AEs and 42 (14%) CEs. The $\theta'/S'/\sigma'$ of these
 178 eddies are near-surface intensified and have relatively smaller amplitudes than those in the first
 179 and second clusters (Figure 2c, 2i, 2o, 2u, 2f, 2l, 2r and 2x). Typical peaking values of $\theta'/S'/\sigma'$ in
 180 this cluster are 1.08 °C, 0.14 psu, and -0.26 kg m⁻³ for AEs, and -0.75 °C, -0.10 psu, and 0.33
 181 kg m⁻³ for CEs. This cluster of eddies is located in the southernmost part of the KOE region and
 182 partially overlapped with the second cluster of eddies in space. These eddies tend to form locally or
 183 originate from the central North Pacific, carrying warm and salty STMW (Supplementary Figures
 184 S1 to S3). To the best of our knowledge, this third eddy cluster has not been documented in the
 185 existing literature. Due to the spatial overlap of the second and third clusters, and the weaker
 186 amplitude of the third cluster, it is difficult to identify the third cluster based on the eddy composite
 187 analysis over a pre-defined region as done in the previous studies (Dong et al., 2017; Ji et al., 2018;
 188 Sun et al., 2017).

189 Finally, it is found that the three distinct eddy clusters in the observations are consistently
 190 reproduced in the reanalysis data (Supplementary Figure S4). The statistical analysis of surface
 191 characteristics within each cluster reveals notable distinctions among them (Supplementary Table
 192 S1 and S2). Moreover, whether including the vertical profile of EKE in the HAC method does not
 193 qualitatively affect the identified eddy clusters in the reanalysis data (Supplementary Figure S5).
 194 In the following analysis, we will focus on the eddy clusters in the reanalysis data as its sample
 195 number of eddies is much larger than that in the observation, yielding a more robust statistic.

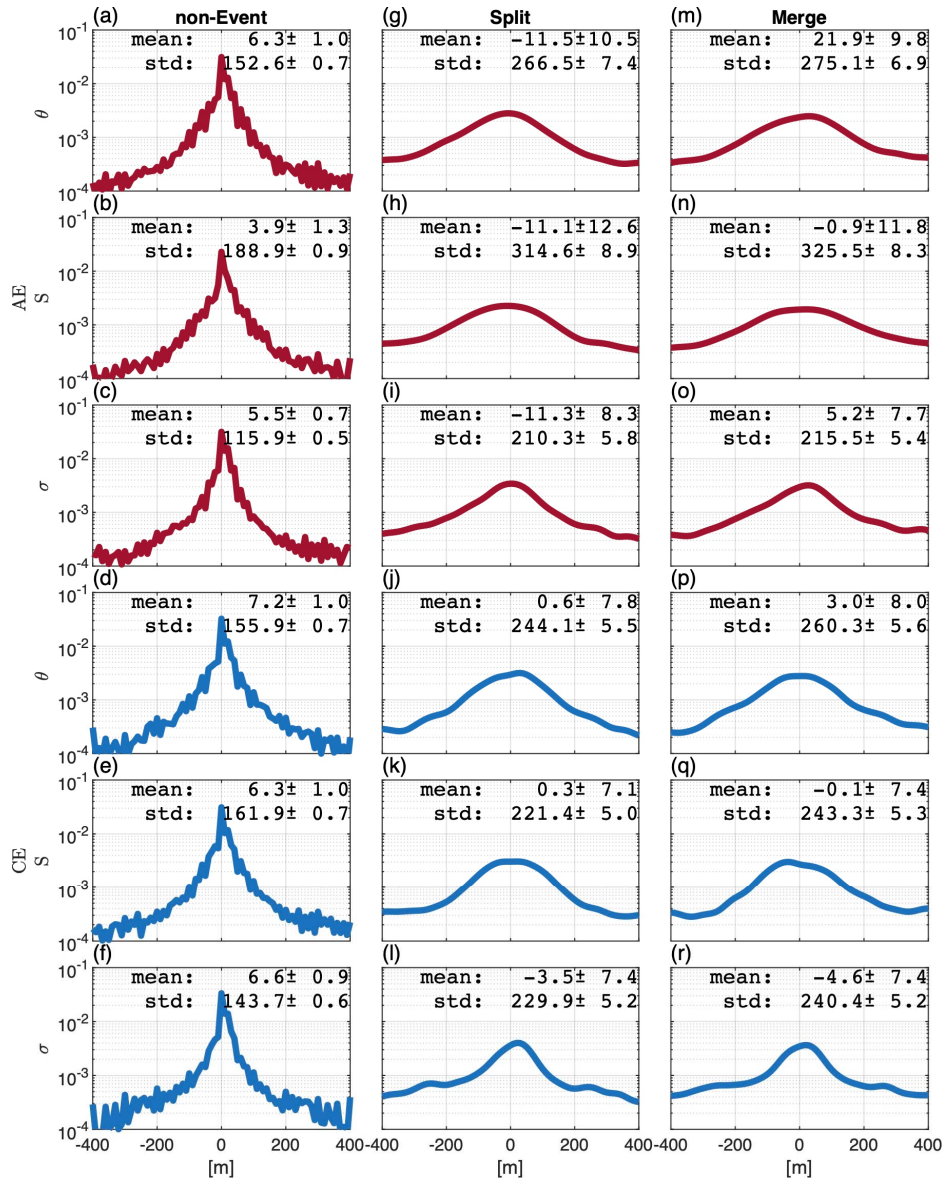
196 3.2 Influences of eddy merging and splitting on vertical structures of mesoscale eddies

197 In the KOE region, displacement and deformation of mesoscale eddies cause frequent eddy
 198 merging and splitting. Among the total 5100 (6371) AEs (CEs) detected in the reanalysis data,
 199 only 2226 (2326) always evolve as a single coherent vortex. The remainings merge with other
 200 eddies or split into multiple eddies sometime during their life cycles. In specific, there are 1624
 201 (2168) AEs (CEs) undergoing merging events and 1250 (1877) undergoing splitting events.

202 To examine the effects of eddy merging and splitting on the eddy vertical structures, we
 203 compute the vertical displacement of peaking depth of σ' during the merging and splitting events
 204 (denoted as d_m and d_s). Here the vertical displacement is estimated as the difference between the
 205 peaking depths of σ' 15 days before and after merging and splitting events. Sensitivity tests
 206 suggest that varying the time span from 10 to 20 days or using the peaking depth of θ' and S' do
 207 not have substantial impacts on the results. It should be noted that the peaking depth of σ' during
 208 a 30-day-long period is likely to change even without the occurrence of eddy merging and
 209 splitting events. Therefore, the values of d_m and d_s should be compared to that when eddy
 210 merging and splitting do not occur (denoted as d_0).

211 Figure 3 presents the probability density functions (PDFs) of d_m , d_s and d_0 . The mean
 212 value and standard deviation of d_0 are 5.5 ± 0.7 (6.6 ± 0.9) m and 115.9 ± 0.5 (143.7 ± 0.6) m for
 213 AEs (CEs), respectively (the errorbars denote the 95% confidence intervals, and hereinafter). The
 214 standard deviation of d_m for AEs (CEs) increases to 215.5 ± 5.4 (240.4 ± 5.2) m, significantly
 215 larger than that of d_0 . Similar is the case for d_s , suggesting that the eddy merging and splitting

216 have notable effects on the eddy vertical structures. Unlike the standard deviation, the difference
 217 among mean values of d_m , d_s and d_0 are minor. It thus suggests that the eddy merging and
 218 splitting should be unlikely to introduce new clusters of eddy vertical structures but instead enlarge
 219 the intra-cluster variability. This is further confirmed by applying the HAC method only to
 220 mesoscale eddies without merging or splitting events. The three re-classified clusters of eddy
 221 vertical structures are qualitatively consistent with those derived from all the eddies
 222 (Supplementary Figure S6).



223
 224 **Figure 3.** Probability density function of vertical displacement of peaking depth of σ' during the eddy merging,
 225 splitting events and otherwise (non-event). The errorbar denotes the 95% confidence intervals of the mean and
 226 standard deviation of vertical displacement.

227 4 Discussion

228 To shed light on the underlying dynamics on the three different clusters of vertical
 229 structures of mesoscale eddies in the KOE region, we perform a linear baroclinic instability (LBI)

230 analysis based on the inviscid quasi-geostrophic potential vorticity (QGPV) equation (Feng et al.,
231 2022).

$$q_t' + \mathbf{U} \cdot \nabla q' + \mathbf{u}' \cdot \nabla Q = 0, \quad -H < z < 0 \#(1.)$$

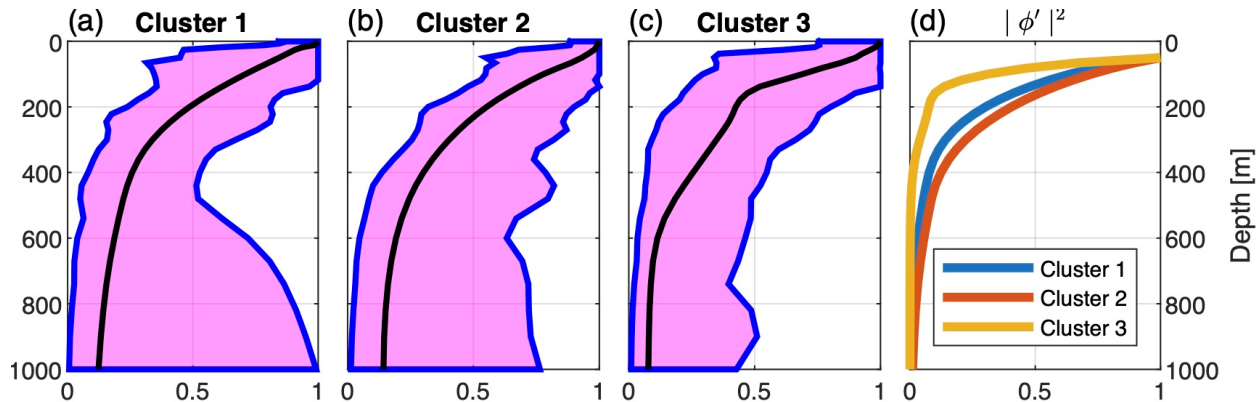
$$\varphi'_{zt} + U \cdot \nabla \varphi'_z + \mathbf{u}' \cdot \nabla (\varphi'_z + f^{-1} N^2 \eta) = 0, \quad z = 0, -H, \#(2.)$$

232 where $\mathbf{U} = U(z)\vec{i} + V(z)\vec{j}$ is the mean current, $Q = \beta y + \vec{k} \cdot \nabla \times U - g/\rho_0 \partial_z (f\rho/N^2)$ is the
233 mean potential vorticity with β the local planetary vorticity gradient, N^2 the background
234 squared buoyancy frequency, ρ_0 the reference density and f the Coriolis parameter,
235 $q' = \nabla^2 \varphi' + \Gamma \varphi'$ is the eddy component of the QGPV with $\Gamma = \partial_z (f^2/N^2 \partial_z)$ the vortex
236 stretching operator, $\mathbf{u}' = -\varphi'_y \vec{i} + \varphi'_x \vec{j}$ is the eddy velocity field expressed in terms of the
237 horizontal eddy streamfunction $\varphi' = \varphi'(x, y, z, t)$, $\varphi'_z = V_z \vec{i} - U_z \vec{j}$ is proportional to the mean
238 horizontal buoyancy gradient via the thermal wind relation, η is the bottom topography height
239 at $z = -H$ and $\eta = 0$ at $z = 0$, and ∇ is the horizontal gradient operator.

240 Contrary to the previous LBI analysis adopting an Eulerian perspective (e.g., Jing et al.,
241 2019), we employ a Lagrangian approach. In specific, the LBI analysis is computed based on the
242 background field at the generation sites of individual eddies. To exclude the mixed-layer
243 baroclinic instability (MLI) generating eddie at submesoscales, the upper boundary is moved from
244 the sea surface to the 50-m depth. The detailed procedures for searching fastest-growing baroclinic
245 instability (BCI) mode at mesoscales can be found in Feng et al. (2021 and 2022).

246 There are, however, several limitations for the LBI analysis. First, it can only account for
247 mesoscale eddies generated primarily via the baroclinic instabilities. Second, it does not take into
248 consideration the variation of eddy vertical structure during the evolution of mesoscale eddies
249 especially the merging and splitting events. Given these limitations, it is unlikely that the
250 variability of eddy vertical structures in the KOE region can be quantitatively reproduced from the
251 LBI analysis. Instead, we attempt to explore whether the three distinct clusters of eddy vertical
252 structures are qualitatively consistent with the inference from the LBI analysis.

253 Figure 4d shows the vertical profiles of $|\varphi'|^2$ associated with mesoscale eddies belonging
254 to different clusters. These vertical profiles can be compared to those of EKE. Although $|\varphi'|^2$ for
255 all the three clusters are surface-intensified, they decay with depth at different rates. The $|\varphi'|^2$ of
256 the first and second clusters has similar e-folding depths 174 m and 217 m), much larger than that
257 (93 m) of the third cluster. This is qualitatively consistent with the decaying rates of EKE for these
258 three clusters (Figure 4a-c). However, we note that although the vertical profiles of $\theta'/S'/\sigma'$ of
259 the first and second clusters are distinct from each other (Figure 2), their vertical profiles of EKE
260 are almost the same. It thus implies that the different vertical eddy structures in the KOE region
261 can only be partially accounted for by the baroclinic instability.



262 **Figure 4.** (a-c) Vertical profiles of normalized EKE for the three clusters in the KOE region. The black curve in
 263 functional boxplot (Genton & Sun, 2020; Sun & Genton, 2011) is the median vertical profile and the magenta box is
 264 the 50% central region. (d) Normalized median vertical profiles of $|\phi'|^2$ derived from the LBI analysis computed at
 265 the generation sites of eddies belonging to the three clusters.
 266

267 5 Conclusions

268 In this study, we utilize a clustering technique to classify the typical vertical structures of
 269 mesoscale eddies in the KOE region based on the observational and reanalysis data. According to
 270 the vertical profiles of $\theta'/S'/\sigma'$, three distinct eddy clusters are identified. The first cluster has
 271 core depths of 100-300 m and is located in the northern part of the KOE. The second and third
 272 clusters has core depths of 300-500 m and 0-100 m, respectively. These two clusters are located in
 273 the southern part of the KOE and overlapped in space. The eddy splitting or merging causes strong
 274 variability of vertical structures of $\theta'/S'/\sigma'$, enlarging their intra-cluster variability.

275 The LBI analysis at the eddy generation sites suggest that the three clusters of eddy vertical
 276 structures can only be partially accounted for by the inference from the baroclinic instabilities.
 277 Further research is needed to better comprehend the underlying dynamics governing the eddy
 278 vertical structures, including the effects of barotropic instability, eddy-mean flow, and eddy-eddy
 279 interactions.

280 Acknowledgments

281 This research was supported by the National Natural Science Foundation of China
 282 (No.41676004). We thank Dr. Laxenaire for providing the TOEddies algorithm code and
 283 application testing.

284 Data Availability Statement

285 The altimeter products were produced and distributed by CMEMS (Copernicus Marine and Environment Monitoring
 286 Service; https://data.marine.copernicus.eu/product/SEALEVEL_GLO_PHY_L4_MY_008_047). The Argo data
 287 used here were provided by the Coriolis Global Data Acquisition Center (GDAC) of France
 288 (ftp://ftp.ifremer.fr/ifremer/argo/geo/pacific_ocean/). The climatological data WOA18 (World Ocean Atlas 2018) is
 289 produced and distributed by NOAA/NCEI (National Centers for Environmental Information;
 290 <https://www.ncei.noaa.gov/products/world-ocean-atlas>). The reanalysis data FORA-WNP30 (Four-dimensional
 291 Variational Ocean ReAnalysis for the Western North Pacific) produced by JAMSTEC (Japan Agency for
 292 Marine-Earth Science and Technology), and JMA/MRI (Meteorological Research Institute, Japan Meteorological

293 Agency) can be downloaded at <https://www.godac.jamstec.go.jp/fora/e/>. The radius of deformation data is calculated
294 and published by Chelton (https://ceos.oregonstate.edu/rossby_radius). The seasonal mean data were processed by
295 SSALTO/DUACS and distributed by AVISO+ (<https://www.aviso.altimetry.fr>) with support from CNES.
296

297 **References**

- 298 Aviso Altimetry. (2022). *SSALTO/DUACS User Handbook: Climatologies products* [dataset].
 299 https://www.aviso.altimetry.fr/fileadmin/documents/data/tools/climatologies_hdbk.pdf
- 300 Cai, M., Liu, M., Qi, H., Cui, Y., Zhang, M., Huang, P., Wang, L., Xie, M., Li, Y., Wang, W., Ke, H., & Liu, F.
 301 (2022). Transport of microplastics in the South China Sea: A review. *Gondwana Research*, *108*, 49–59.
 302 <https://doi.org/10.1016/j.gr.2021.12.003>
- 303 Chaigneau, A., Eldin, G., & Dewitte, B. (2009). Eddy activity in the four major upwelling systems from satellite
 304 altimetry (1992–2007). *Progress in Oceanography*, *83*(1–4), 117–123.
 305 <https://doi.org/10.1016/j.pocean.2009.07.012>
- 306 Chaigneau, A., Gizolme, A., & Grados, C. (2008). Mesoscale eddies off Peru in altimeter records: Identification
 307 algorithms and eddy spatio-temporal patterns. *Progress in Oceanography*, *79*(2–4), 106–119.
 308 <https://doi.org/10.1016/j.pocean.2008.10.013>
- 309 Ding, Y., & Jing, C. (2020). Three-dimensional thermohaline anomaly structures of rings in the Kuroshio Extension
 310 region. *Acta Oceanologica Sinica*, *39*(3), 25–35. <https://doi.org/10.1007/s13131-020-1559-3>
- 311 Dong, D., Brandt, P., Chang, P., Schütte, F., Yang, X., Yan, J., & Zeng, J. (2017). Mesoscale Eddies in the
 312 Northwestern Pacific Ocean: Three-Dimensional Eddy Structures and Heat/Salt Transports. *Journal of*
 313 *Geophysical Research: Oceans*, *122*(12), 9795–9813. <https://doi.org/10.1002/2017JC013303>
- 314 Du, T., Jing, Z., Wu, L., Wang, H., Chen, Z., Ma, X., Gan, B., & Yang, H. (2022). Growth of ocean thermal energy
 315 conversion resources under greenhouse warming regulated by oceanic eddies. *Nature Communications*, *13*(1),
 316 7249. <https://doi.org/10.1038/s41467-022-34835-z>
- 317 Fassbender, A. J., Sabine, C. L., Cronin, M. F., & Sutton, A. J. (2017). Mixed-layer carbon cycling at the Kuroshio
 318 Extension Observatory. *Global Biogeochemical Cycles*, *31*(2), 272–288.
 319 <https://doi.org/10.1002/2016GB005547>
- 320 Feng, L., Liu, C., Köhl, A., Stammer, D., & Wang, F. (2021). Four Types of Baroclinic Instability Waves in the
 321 Global Oceans and the Implications for the Vertical Structure of Mesoscale Eddies. *Journal of Geophysical*
 322 *Research: Oceans*, *126*(3). <https://doi.org/10.1029/2020JC016966>
- 323 Feng, L., Liu, C., Köhl, A., & Wang, F. (2022). Seasonality of Four Types of Baroclinic Instability in the Global
 324 Oceans. *Journal of Geophysical Research: Oceans*, *127*(5). <https://doi.org/10.1029/2022JC018572>
- 325 Genton, M. G., & Sun, Y. (2020). Functional Data Visualization. In N. Balakrishnan, T. Colton, B. Everitt, W.
 326 Piegorisch, F. Ruggeri, & J. L. Teugels (Eds.), *Wiley StatsRef: Statistics Reference Online* (1st ed., pp. 1–11).
 327 Wiley. <https://doi.org/10.1002/9781118445112.stat08290>
- 328 Gilchrist, R. M., Hall, R. A., Bacon, J. C., Rees, J. M., & Graham, J. A. (2020). Increased dispersion of oil from a
 329 deep water seabed release by energetic mesoscale eddies. *Marine Pollution Bulletin*, *156*, 111258.
 330 <https://doi.org/10.1016/j.marpolbul.2020.111258>
- 331 Gladyshev, S., Talley, L., Kantakov, G., Khen, G., & Wakatsuchi, M. (2003). Distribution, formation, and seasonal
 332 variability of Okhotsk Sea Mode Water. *Journal of Geophysical Research: Oceans*, *108*(C6).
 333 <https://doi.org/10.1029/2001JC000877>
- 334 Ji, J., Dong, C., Zhang, B., Liu, Y., Zou, B., King, G. P., Xu, G., & Chen, D. (2018). Oceanic Eddy Characteristics
 335 and Generation Mechanisms in the Kuroshio Extension Region. *Journal of Geophysical Research: Oceans*,
 336 *123*(11), 8548–8567. <https://doi.org/10.1029/2018JC014196>
- 337 Jing, Z., Chang, P., Shan, X., Wang, S., Wu, L., & Kurian, J. (2019). Mesoscale SST Dynamics in the Kuroshio–
 338 Oyashio Extension Region. *Journal of Physical Oceanography*, *49*(5), 1339–1352.
 339 <https://doi.org/10.1175/JPO-D-18-0159.1>
- 340 Jing, Z., Wang, S., Wu, L., Chang, P., Zhang, Q., Sun, B., Ma, X., Qiu, B., Small, J., Jin, F.-F., Chen, Z., Gan, B.,
 341 Yang, Y., Yang, H., & Wan, X. (2020). Maintenance of mid-latitude oceanic fronts by mesoscale eddies.
 342 *Science Advances*, *6*(31), eaba7880. <https://doi.org/10.1126/sciadv.aba7880>
- 343 Laxenaire, R., Speich, S., Blanke, B., Chaigneau, A., Pegliasco, C., & Stegner, A. (2018). Anticyclonic Eddies
 344 Connecting the Western Boundaries of Indian and Atlantic Oceans. *Journal of Geophysical Research: Oceans*,
 345 *123*(11), 7651–7677. <https://doi.org/10.1029/2018JC014270>
- 346 Laxenaire, R., Speich, S., & Stegner, A. (2019). Evolution of the Thermohaline Structure of One Agulhas Ring
 347 Reconstructed from Satellite Altimetry and Argo Floats. *Journal of Geophysical Research: Oceans*, *124*(12),
 348 8969–9003. <https://doi.org/10.1029/2018JC014426>

- 349 Laxenaire, R., Speich, S., & Stegner, A. (2020). Agulhas Ring Heat Content and Transport in the South Atlantic
350 Estimated by Combining Satellite Altimetry and Argo Profiling Floats Data. *Journal of Geophysical Research:*
351 *Oceans*, 125(9). <https://doi.org/10.1029/2019JC015511>
- 352 Masuzawa, J. (1969). Subtropical mode water. *Deep Sea Research and Oceanographic Abstracts*, 16(5), 463–472.
353 [https://doi.org/10.1016/0011-7471\(69\)90034-5](https://doi.org/10.1016/0011-7471(69)90034-5)
- 354 McGillicuddy, D. J., Anderson, L. A., Bates, N. R., Bibby, T., Buesseler, K. O., Carlson, C. A., Davis, C. S., Ewart,
355 C., Falkowski, P. G., Goldthwait, S. A., Hansell, D. A., Jenkins, W. J., Johnson, R., Kosnyrev, V. K., Ledwell,
356 J. R., Li, Q. P., Siegel, D. A., & Steinberg, D. K. (2007). Eddy/Wind Interactions Stimulate Extraordinary
357 Mid-Ocean Plankton Blooms. *Science*, 316(5827), 1021–1026. <https://doi.org/10.1126/science.1136256>
- 358 McGillicuddy, D. J., Robinson, A. R., Siegel, D. A., Jannasch, H. W., Johnson, R., Dickey, T. D., McNeil, J.,
359 Michaels, A. F., & Knap, A. H. (1998). Influence of mesoscale eddies on new production in the Sargasso Sea.
360 *Nature*, 394(6690), 263–266. <https://doi.org/10.1038/28367>
- 361 Nakano, H., Tsujino, H., Sakamoto, K., Urakawa, S., Toyoda, T., & Yamanaka, G. (2018). Identification of the
362 fronts from the Kuroshio Extension to the Subarctic Current using absolute dynamic topographies in satellite
363 altimetry products. *Journal of Oceanography*, 74(4), 393–420. <https://doi.org/10.1007/s10872-018-0470-4>
- 364 Oka, E., Kouketsu, S., Toyama, K., Uehara, K., Kobayashi, T., Hosoda, S., & Suga, T. (2011). Formation and
365 Subduction of Central Mode Water Based on Profiling Float Data, 2003–08. *Journal of Physical*
366 *Oceanography*, 41(1), 113–129. <https://doi.org/10.1175/2010JPO4419.1>
- 367 Pegliasco, C., Chaigneau, A., & Morrow, R. (2015). Main eddy vertical structures observed in the four major
368 Eastern Boundary Upwelling Systems. *Journal of Geophysical Research: Oceans*, 120(9), 6008–6033.
369 <https://doi.org/10.1002/2015JC010950>
- 370 Pujol, M.-I. (2022). *PRODUCT USER MANUAL For Sea Level Altimeter products* [dataset]. Copernicus Marine
371 Service. <https://doi.org/10.48670/moi-00148>
- 372 Qiu, B., & Chen, S. (2010). Eddy-mean flow interaction in the decadal modulating Kuroshio Extension system.
373 *Deep Sea Research Part II: Topical Studies in Oceanography*, 57(13–14), 1098–1110.
374 <https://doi.org/10.1016/j.dsr2.2008.11.036>
- 375 Saito, H., Suga, T., Hanawa, K., & Watanabe, T. (2007). New type of pycnostad in the western subtropical-subarctic
376 transition region of the North Pacific: Transition Region Mode Water. *Journal of Oceanography*, 63(4), 589–
377 600. <https://doi.org/10.1007/s10872-007-0052-3>
- 378 Sambe, F., & Suga, T. (2022). Unsupervised Clustering of Argo Temperature and Salinity Profiles in the
379 Mid-Latitude Northwest Pacific Ocean and Revealed Influence of the Kuroshio Extension Variability on the
380 Vertical Structure Distribution. *Journal of Geophysical Research: Oceans*, 127(3), e2021JC018138.
381 <https://doi.org/10.1029/2021JC018138>
- 382 Sun, W., Dong, C., Wang, R., Liu, Y., & Yu, K. (2017). Vertical structure anomalies of oceanic eddies in the
383 Kuroshio Extension region. *Journal of Geophysical Research: Oceans*, 122(2), 1476–1496.
384 <https://doi.org/10.1002/2016JC012226>
- 385 Sun, Y., & Genton, M. G. (2011). Functional Boxplots. *Journal of Computational and Graphical Statistics*, 20(2),
386 316–334. <https://doi.org/10.1198/jcgs.2011.09224>
- 387 Usui, N., Wakamatsu, T., Tanaka, Y., Hirose, N., Toyoda, T., Nishikawa, S., Fujii, Y., Takatsuki, Y., Igarashi, H.,
388 Nishikawa, H., Ishikawa, Y., Kuragano, T., & Kamachi, M. (2017). Four-dimensional variational ocean
389 reanalysis: A 30-year high-resolution dataset in the western North Pacific (FORA-WNP30). *Journal of*
390 *Oceanography*, 73(2), 205–233. <https://doi.org/10.1007/s10872-016-0398-5>
- 391 Ward, J. H. (1963). Hierarchical Grouping to Optimize an Objective Function. *Journal of the American Statistical*
392 *Association*, 58(301), 236–244. <https://doi.org/10.1080/01621459.1963.10500845>
- 393 Yang, H., Qiu, B., Chang, P., Wu, L., Wang, S., Chen, Z., & Yang, Y. (2018). Decadal Variability of Eddy
394 Characteristics and Energetics in the Kuroshio Extension: Unstable Versus Stable States. *Journal of*
395 *Geophysical Research: Oceans*, 123(9), 6653–6669. <https://doi.org/10.1029/2018JC014081>
- 396 Yasuda, I. (1997). The origin of the North Pacific Intermediate Water. *Journal of Geophysical Research: Oceans*,
397 102(C1), 893–909. <https://doi.org/10.1029/96JC02938>
- 398 Yu, X., Naveira Garabato, A. C., Martin, A. P., Buckingham, C. E., Brannigan, L., & Su, Z. (2019). An Annual
399 Cycle of Submesoscale Vertical Flow and Restratification in the Upper Ocean. *Journal of Physical*
400 *Oceanography*, 49(6), 1439–1461. <https://doi.org/10.1175/JPO-D-18-0253.1>